Retrieval of nearshore bathymetry from Landsat 8 images: a tool for coastal monitoring in shallow waters

Pacheco, A.[1], Horta, J.[1], Loureiro, C.[1, 2, 3], Ferreira, Ó.[1]

[1]CIMA/Universidade do Algarve, Edifício 7, Campus de Gambelas Faro, 8005-139, Portugal,
[2] Marine Geology Research Unit, School of Agriculture, Earth and Environmental Sciences, University of KwaZulu-Natal, Westville Campus, Private Bag X54001, Durban, South Africa
[3] Environmental Sciences Research Institute, School of Environmental Sciences, University of Ulster, Coleraine, BT52 1SA, United Kingdom
ampacheco@ualg.pt, jphorta@ualg.pt, cloureiro@ualg.pt, oferreir@ualg.pt

Abstract

Nearshore bathymetry is likely to be the coastal variable that most limits the investigation of coastal processes and the accuracy of numerical models in coastal areas, as acquiring medium spatial resolution data in the nearshore is highly demanding and costly. As such, the ability to derive bathymetry using remote sensing techniques is a topic of increasing interest in coastal monitoring and research. This contribution focuses on the application of the linear transform algorithm to obtain satellite-derived bathymetry (SDB) maps of the nearshore, at medium resolution (30 m), from freely available and easily accessible Landsat 8 imagery. The algorithm was tuned with available bathymetric Light Detection and Ranging (LiDAR) data for a 60-km-long nearshore stretch of a highly complex coastal system that includes barrier islands, exposed sandy beaches, and tidal inlets (Ria Formosa, Portugal). A comparison of the retrieved depths is presented, enabling the configuration of nearshore profiles and extracted isobaths to be explored and compared with traditional topographic/bathymetric techniques (e.g., high- and medium-resolution LiDAR data and survey-grade echo-sounding combined with high-precision positioning systems). The results demonstrate that the linear algorithm is efficient for retrieving bathymetry from multi-spectral satellite data for shallow water depths (0 to 12 m), showing a mean bias of −0.2 m, a median difference of −0.1 m, and a root mean square error of 0.89 m. Accuracy is shown to be depth dependent, an inherent limitation of passive optical detection systems. Accuracy further decreases in areas where turbidity is likely to be higher, such as locations adjacent to tidal inlets. The SDB maps provide reliable estimations of the shoreline position and of nearshore isobaths for different cases along the complex coastline analysed. The use of freely available satellite imagery proved to be a quick and reliable method for acquiring updated medium-resolution, high-

frequency (days and weeks), low-cost bathymetric information for large areas and depths of up to 12 m in clear waters without wave breaking, allowing almost constant monitoring of the submerged beach and the shoreface.

Keywords: Satellite-derived bathymetry; Landsat; LiDAR; linear transform algorithm; coastal monitoring; Ria Formosa

1. Introduction

Updated and detailed coastal topography and bathymetry are increasingly being required for a wide variety of purposes including research, management, and marine spatial planning. With the expansion of coastal and marine economic activities, there is a growing need to develop fast and accurate measurements of nearshore regions, as well as to describe the physical features of the sea bottom and adjoining coastal areas, particularly for the purposes of modelling and monitoring. Coastal observation systems continue to be developed for measuring parameters of and processes related to water quality, hydrodynamics, meteorology, and ecology, as well as submarine geomorphology (analysed using bathymetric data).

Accurate bathymetries are the most essential data for driving coastal modelling and monitoring. Currently, two of the most widely used techniques for acquiring bathymetric data rely on single- or multi-beam echo-sounding and airborne Light Detection and Ranging (LiDAR). However, the cost and logistical difficulties of obtaining nearshore bathymetry using these methods makes survey updates rare or allows them to be conducted only on sites of special interest. As such, the ability to derive continuous bathymetry from satellite images has become a topic of increased interest for coastal monitoring. Such an approach exploits the fact that different wavelengths of the light spectrum are attenuated by water to varying degrees. Initially, these approaches could not be used for marine mapping applications owing to the unique optical properties of water and to highly variable parameters such as turbidity. However, advances in the optical sensors on board remote sensing satellite platforms have improved the ability to detect the spectral properties of aquatic targets such as bottom reflectance, which can then be inverted to yield direct estimates of depth (Mobley et al., 2005).

The present work explores the retrieval of satellite-derived bathymetry (SDB) for shallow coastal areas, aiming to provide a straightforward and inexpensive method for obtaining and updating bathymetric data relevant to coastal research and management. The study takes advantage of several improvements introduced in the latest generation of Landsat imagery that were included in the Landsat 8 mission launched in early 2013. Furthermore, the Landsat 8 satellite images the entire Earth at approximately fortnightly intervals (every 16 days) and the data collected by the instruments onboard the satellite are available to download at no charge. This paper details the processing of the satellite images required to derive bathymetric maps using the water radiance of three bands (coastal aerosol: 433–453 nm; blue: 450–515 nm; and green: 525–600 nm). The processing steps include the radiometric rescaling of the images, the application of adapted Lyzenga's (1985) depth-retrieval algorithm that uses existing bathymetric data for tuning the image-to-depth conversion, and an averaged and depth-dedicated error analysis. The SDB maps generated have medium resolution (~30 m) and are used to provide cost-effective, frequent, high-density data in raster map format.

2. Study area

The nearshore coastal waters adjacent to the Ria Formosa system in southern Portugal were chosen as the test case in which to derive satellite bathymetric maps (Fig. 1A) because of the complexity and variability of this coastal environment. The Ria Formosa is a coastal lagoon bordered by a multi-inlet barrier island system, and the adjacent coastal areas have several different morphologies such as tidal inlets, alongshore bars, crescentic bars, shoals, and ebb channels. The total length of the system is 60 km, presently comprising five islands and two peninsulas separated by six tidal inlets. The inlets comprise three artificially opened or relocated inlets (Ancão, Fuseta, and Lacém), two artificially stabilised inlets (Faro–Olhão and Tavira), and one natural inlet (Armona). Tides in the area are semi-diurnal, with average ranges of 2.8 m and 1.3 m for spring and neap tides, respectively. Maximum ranges of 3.5 m can be reached during spring tides. Wave energy is moderate with an average annual offshore significant wave height (H_s) of 1.0 m and an average peak period (T_p) of 8.2 s. Dominant incident waves are from the W–SW, representing 71% of occurrences, although E–SE conditions represent 23% of the observations (Costa et al., 2001). Net littoral drift and alongshore currents are typically from west to east. The cuspate shape of this coastal area induces two behaviours in terms of exposure to wave action: the west coast is more energetic, being under the direct influence of the dominant wave conditions (W–SW), whereas the east coast is directly exposed only to the E–SE waves. The nearshore morphology also reflects this cuspate shape, with the bathymetry being generally shore parallel, although incorporating complex areas such as shoals, ebb deltas, alongshore and swash bars, and ridge and runnel systems (Pacheco et al., 2011).

3. METHODS

3.1. Physical assumptions

The physical concept underlying the ability to estimate bathymetry from multi-spectral imagery is the wavelength-dependent attenuation of light in the water column. The transformation of subsurface reflectance to the bottom albedo is based on analytical equations for irradiance reflectance (R) and remote-sensing reflectance (R_{rs}) for both deep- and shallow-water applications parameterised by Albert and Mobley (2003). In shallow waters, R_{rs} is the fundamental property for the inversion of subsurface properties such as water depth or bottom composition. R_{rs} depends not only on the absorption and scattering properties of dissolved and suspended material in the water column, but also on the bottom depth (d_b) and the reflectivity of the bottom, or the bottom albedo (R_B) (Albert & Mobley, 2003; Dekker et al., 2011). The spectral R_{rs} is given by:

$$R_{rs}(\lambda) = f[a(\lambda), b_b(\lambda), R_B(\lambda), d_b, \theta_w, \theta_v, \varphi] \quad (1)$$

where $a(\lambda)$ is the absorption coefficient, $b_b(\lambda)$ is the backscatter coefficient, $R_B(\lambda)$ is the benthic spectral reflectance (i.e., bottom albedo), d_b is the bottom depth, θ_w is the sub-surface solar zenith angle, θ_v is the sub-surface viewing angle from nadir, and φ is the viewing azimuth angle from the solar plane. The result is a complete set of analytical equations for the remote sensing signals R and R_{rs} in both deep and shallow waters (Albert and Mobley, 2003; Albert and Gege, 2006). The input variables for the parameterisation are the inherent optical properties of the water mentioned above, that is, $a(\lambda)$ and $b_b(\lambda)$. Additionally, θ_w and θ_v are considered.

3.2. Dataset

The Landsat 8 satellite images consist of 11 spectral bands providing moderate-resolution (15–100 m) imagery of Earth's land surface. The spatial resolution of the spectral bands is 30 m for Bands 1 to 7 and 9, 15 m for Band 8 (panchromatic), and 100 m for Bands 10 and 11. The approximate scene size is 170 km north–south by 183 km east–west. Landsat 8 has many differences compared with previous Landsat missions. Particularly relevant was the introduction of the new band 1 (ultra-blue and/or coastal aerosol), which is useful for coastal studies. Further details on Landsat 8 products and scientific applications can be found in Roy et al. (2014). The standard Landsat 8 products provided by the United States Geological Survey (USGS) consist of quantised and calibrated Digital Numbers (DNs) representing multi-spectral image data acquired with both the Operational Land Imager (OLI) and the Thermal Infra-Red Sensor (TIRS). The products are delivered in 16-bit unsigned integer format and can be rescaled to Top Of Atmosphere (TOA) reflectance and/or radiance using radiometric rescaling coefficients provided in the product metadata file (MTL file). Two satellite scenes from April and June 2013 were downloaded based on survey time, geographic extent, and environmental conditions (e.g., an absence of cloud cover), and were georeferenced to the WGS84 datum, UTM projection Zone 29 (Table 1).

To tune the satellite image-to-depth conversion, up-to-date and detailed bathymetric information was obtained from the May 2011 topographic–bathymetric LiDAR dataset of the Portuguese coast, with the subset of waters in the Ria Formosa system being of particular interest (Table 1). The combined topographic and bathymetric LiDAR datasets were assembled to produce a model of the Portuguese coastal areas with 2-m resolution from 0 to 12 m depth, confirmed to Order 1A of the International Hydrographic Organisation standards s44 (2008). For the present study, XY positions from all the acquired survey data were also projected using UTM Zone 29, referred to the GRS 80 ellipsoid and to the WGS84 datum. Depth (Z) measurements were referred to mean sea level (MSL).

3.3. Depth-retrieval algorithm

The method that was used to derive bathymetry from variable bottom types is an adapted version of the linear transform bathymetry algorithm originally developed by

Lyzenga (1978, 1985) and was applied to the Landsat 8 scene to match with the available LiDAR bathymetric reference dataset. The method uses the reflectance for each satellite imagery band, calculated with the sensor calibration files and corrected for atmospheric effects. The reflectance of water (R_w), which includes the bottom where the water is optically shallow, is given by:

$$R_w = \frac{\pi L_w(\lambda)}{E_d(\lambda)} \tag{2}$$

where L_w is the water-leaving radiance, E_d is the downwelling irradiance entering the water, and λ is the spectral band. L_w and R_w refer to values above the water surface. R_w is determined by correcting the total reflectance R_T for aerosol and surface reflectance, as estimated by the near-IR band, and for the Rayleigh reflectance R_r by:

$$R_w = R_T(\lambda_i) - Y(\lambda_i)R_T(\lambda_{IR}) - R_r(\lambda_i) \tag{3}$$

where Y is the constant to correct the spectral variation and is aerosol dependent, subscript i denotes a visible channel, and subscript IR denotes the near-IR (NIR) channel. R_T is found by:

$$R_T(\lambda_i) = \frac{\pi L_T(\lambda_i)/E_0(\lambda_i)}{(1/r^2)T_0(\lambda_i)T_1(\lambda_i)cos\theta_0} \tag{4}$$

where L_T is the (total) radiance measured at the satellite, E_0 is the solar constant, r is the Earth–Sun distance in astronomical units, θ_0 is the solar zenith angle, and T_0 and T_1 are the transmission coefficients for Sun-to-Earth and Earth-to-satellite, respectively (Stumpf et al., 2003).

The atmosphere has a significant impact on satellite data, such as information loss, caused by scattering by atmospheric constituents and aerosols. Atmospheric correction over coastal waters is particularly challenging because of the much lower signal-to-noise ratio (SNR) compared with that of land. Consequently, water-specific Landsat 8 atmospheric correction techniques are being developed that take advantage of the new shorter-wavelength coastal blue band (Roy et al., 2014).

For Landsat 8, the number of steps necessary in the atmospheric correction process can be reduced when compared with previous Landsat missions because terms have been embedded in Landsat 8 DN values. For the present paper, atmospheric corrections were performed using the Dark Object Subtraction (DOS) method. DOS assumes that dark objects (e.g., deep water and shadows) have near-zero-percent reflectance. Thus, the signal recorded by the sensor from these features includes a substantial component of atmospheric scattering, which must be removed (Chavez, 1988, 1996). The basic assumption is that within the image, some pixels are in complete shadow and their radiances received at the satellite are due to atmospheric scattering (i.e., path radiance, Chavez, 1996). This assumption is combined with the fact that very few targets on Earth's surface are absolutely black. In the present study, the minimum scatter radiance (i.e., the 1% radiance of a dark object) was determined (Nazeer et al., 2014) as:

$$L_{1\%} = \frac{0.01 E_{sun\lambda_i} cos\theta_0}{\pi d^2} \tag{5}$$

where $E_{sun\lambda_i}$ is the exo-atmospheric solar irradiance for band λ_i (Wm^{-2}μm^{-1}), and d is the Earth–Sun distance (in astronomical units). The value $L_{1\%}$ was then subtracted from each corresponding $L_T(\lambda_i)$ to remove the path radiance. This method has an advantage over other methods as it does not require any in situ atmospheric information and has been consistently used for atmospheric corrections of multi-spectral imagery in diverse coastal settings (Keith et al., 2014). Recent evaluations have confirmed the performance of the DOS method for precise atmospheric corrections of Landsat imagery over coastal areas (Nazeer et al., 2014).

Following Lyzenga (1978, 1985) and Stumpf et al. (2003), two or more bands can provide an independent correction for bottom albedo in finding the depth as well as a linear solution between satellite-derived depth (Z_{LSat8}) and water reflectance, which is given by:

$$Z_{LSat8} = a_0 + a_i(X_i) + a_j(X_j) + a_K(X_K) \tag{6}$$

where

$$X_i = \ln\left[R_w(\lambda_i) - R_\infty(\lambda_i)\right] \tag{7}$$

$$X_j = \ln\left[R_w(\lambda_j) - R_\infty(\lambda_i)\right] \tag{8}$$

$$X_k = \ln\left[R_w(\lambda_k) - R_\infty(\lambda_i)\right] \tag{9}$$

where R_∞ is the water column reflectance in the case where the water is optically deep (presumed to be min(R_w) in optically deep water, following Lyzenga, 1985). R_∞ and the constants a_0, a_i, a_j, and a_k are determined by multiple linear regression computed using the LiDAR bathymetric data (Z_{LiDAR}) for depths of 0–12 m; $i, j,$ and k are the indices representing the coastal aerosol, blue, and green bands (λ) of Landsat 8 scenes, respectively.

To apply the multiple linear regression, the LiDAR data from May 2011 were extracted for the entire nearshore Ria Formosa area with 30-m resolution at exactly the same points as were the data retrieved by the Landsat 8 image of June 2013, comprising a total of 35,247 points (N). A limitation of this comparison is the fact that Landsat 8 scenes of Ria Formosa have been available only since early 2013, whereas the depth-retrieval linear algorithm applied to the Landsat 8 June 2013 scenes to derive the SDB maps was tuned with a LiDAR bathymetric dataset from May 2011; that is, there is a 2-year difference. Therefore, a perfect agreement between SDB and LiDAR maps is not expected, given that morphological differences are likely to occur in a moderately energetic nearshore system comprising barrier islands and tidal inlets exposed to dynamic oceanographic conditions, and given that (in the case of adjacent areas of tidal inlets) dredging activities have taken place in the main navigable channels or ebb deltas. However, the number of points (N) retrieved and the fact that the analysis covers a 60-km-long coastal stretch ensure the robustness of the statistical comparison as a large number of Z points extracted at medium resolution are expected to remain unchanged. Moreover, the satellite image and the LiDAR data were both obtained in late spring (June 2013 and May 2011, respectively), implying that the main morphologies should be adjusted to similar energy conditions.

LiDAR data points were referenced to MSL and were tide corrected, but the satellite image was acquired at a particular date and time. As such, a corresponding tide offset needs to be corrected before applying the regression model to obtain model coefficients. The correction of the satellite image was performed by matching the image time with tidal level using a tidal predictor (Pawlowicz et al., 2002). The processing steps are illustrated in Fig. 2.

3.4. Data analysis

The satellite-derived depths (Z_{LSat8}) were compared against the LiDAR depths (Z_{LiDAR}) and separated into depth ranges (Table 2 and Fig. 3). The differences between Z_{LSat8} and Z_{LiDAR} were then analysed statistically (Table 2 and Fig. 4) and plotted against the X coordinate to evaluate their spatial variation throughout the study area (Fig. 3). During the calibration stage, and to better understand the coastal morphologies that SDB with a resolution of 30 m could distinguish, bathymetric charts were derived for particular areas of interest (AoI). AoI1 represents the Ancão Peninsula (Fig. 1) and includes: Bm1, a bathymetric map with 2-m resolution using the LiDAR high-resolution data (Fig. 5A); Bm2, a bathymetric map with 30-m resolution obtained from a resampling of the LiDAR data, which constitutes the reference dataset used for determining the constants a_0, a_i, a_j, and a_k in the multiple linear regression (Eq. 6 and Fig. 5B); and Bm3, the SDB map (Fig. 5C).

The same interpolator was used to grid the bathymetric maps within the same limits and resolution following quality controls suggested by Hicks and Hume (1997). Differences between Bm2 and Bm3 were then determined by applying the difference map method (DMM) described by Stauble (1998) (Fig. 5D). The DMM is a straightforward method for computing vertical changes in cells by subtracting two comparison surfaces. An output map (hereafter referred to as "DMM") is then created with the differences in Z between surveys, which is used to evaluate the relative error of the SDB against the LiDAR survey, namely, by assessing the spatial distribution of error and its association with specific morphological features (e.g., swash bars, isobaths, and inlet channels). Complementing this, three descriptive statistical parameters for assessing the overall performance of the depth-retrieval algorithm were computed (Brando et al., 2009):

$$Bias(Z_{LSat8}, Z_{LiDAR}) = mean(Z_{LSat8}) - mean(Z_{LiDAR}) \quad (10)$$

$$DifMedian(Z_{LSat8}, Z_{LiDAR}) = median(Z_{LSat8}) - median(Z_{LiDAR}) \quad (11)$$

$$RMSE(Z_{LSat8}) = \sqrt{Var(Z_{LSat8}) + (Bias(Z_{LSat8}, Z_{LiDAR}))^2} \quad (12)$$

where Z_{LiDAR} is the LiDAR depth (from the 30-m-resolution resampled LiDAR dataset) and Z_{LSat8} is the depth estimated by applying inversion techniques to the Landsat 8 multi-spectral data (i.e., the SDB, Fig. 2). $Bias$ (m) and $DifMedian$ (m) provide the relative accuracy in the measurement, whereas $RMSE$ (Root Mean Square Error, m) includes both random errors (i.e., affecting the precision of the measurement) and systematic errors (i.e., affecting the accuracy of the measurement) (Table 3). Twelve cross-shore profiles spaced every 1000 m (P1 to P12, shown in Fig. 5D) were then extracted from Bm1, Bm2, and Bm3 to evaluate the performance of the SDB map in characterizing the nearshore morphological profile when compared with the high-resolution LiDAR bathymetry (Bm1) and with the coarser grid resolution resample from the LiDAR bathymetric data (Bm2). Such nearshore profiles are represented in Fig. 6, whereas a comparison of the 2-m, 4-m, 6-m, and 8-m isobaths extracted from Bm1, Bm2, and Bm3 is presented in Fig. 7.

AoI2 comprises the easternmost area of Tavira Island, the Tavira Inlet, and the westernmost area of Cabanas Island (Fig. 1C), and was chosen for several reasons. First, as mentioned above, Ria Formosa has a cuspate shape, and whereas AoI1 faces the prevailing SW oceanographic conditions, AoI2 faces the E–SE conditions. Second, whereas AoI1 encloses an artificially opened inlet that has been allowed to migrate naturally (Ancão Inlet), AoI2 encloses a stabilised inlet with two jetties (Tavira Inlet). A similar procedure to that used for AoI1 was adopted for analysing AoI2, and three bathymetric maps were derived: Bm1, a bathymetric map with 2-m resolution using the LiDAR high-resolution data (Fig. 8A); Bm2, a bathymetric map with 30-m resolution using the resampled LiDAR data (Fig. 8B); and Bm3, the SDB map (Fig. 8C). Differences between Bm2 and Bm3 were then determined by applying the DMM (Fig. 8D). Univariate statistics of the DMM for each AoI are presented in Table 3. Because nearshore dynamics and morphological changes are assessed primarily by analysing variation in the nearshore profiles, cross-shore profiles spaced every 1000 m were also extracted from the bathymetric maps (i.e., from Bm1, Bm2, and Bm3) of AoI2 (Fig. 8D). The cross-shore nearshore profiles are shown in Fig. 9, and the isobaths extracted from Bm1, Bm2, and Bm3 are displayed in Fig. 10.

After calibrating and tuning the coefficients, two validation areas were selected and independently surveyed: AoI3, Barreta Island bathymetry (Fig. 1) obtained on 26 April 2013; and AoI4, a bathymetry survey performed on 30 April 2013 at Tavira Inlet. Both bathymetries were compared with SDB maps created using the above-determined coefficients applied to a different Landsat 8 scene obtained for the closest possible date to the surveys (26 April 2013, Table 1). The bathymetries of both AoI3 and AoI4 were established using a Real-Time Kinematics–Differential Global Positioning System (RTK–DGPS) synchronised with a single-beam survey-grade echo-sounder, the Echotrac CV100 (Odom Hydrographic System, Inc.) with a 200-kHz transducer. The echo-sounding bathymetries were performed under fair-weather southwesterly conditions. The datasets were collected to represent typical environments encountered in a bathymetric analysis of nearshore and coastal inlets, including complex morphologies such as ebb deltas and swash bars. Survey lines were spaced 25 m apart, with survey positions being referenced to the European Terrestrial Reference System 1989 (ETRS89) and depth measurements being referred to MSL. More details on equipment, data acquisition, and data processing are given by Horta et al. (2014). Both echo-sounder + RTK–DGPS survey datasets were gridded at Landsat 8′ resolution (i.e., 30 m, Figs 11A and 12A). The SDB maps were determined with the coefficients calculated using Eq. 6 (Figs. 11B and 12B). For the purpose of comparison, a DMM grid was produced to determine volumetric variations (Figs 11C and 12C). The spatial differences between the LiDAR and SDB maps were first evaluated visually by analysing the elevation-difference maps and afterwards by computing univariate statistics (Table 3).

4. Results

4.1. Depth-retrieval algorithm

The spatial distribution of the residuals (N = 35,247) between depths determined using the depth-retrieval linear algorithm applied to the Landsat 8 scene (June 2013) and those acquired using LiDAR (May 2011) over 60 km of the nearshore are shown visually in Fig. 3 and given statistically in Table 2. The depth data were separated into 2-m classes to allow both methods' strengths and limitations to be distinguished. The distribution of frequencies was determined to analyse differences between satellite-derived depth (Z_{LSat8}) and LiDAR depth (Z_{LiDAR}) for each 2-m depth class (Fig. 4). Overall, and for all depth classes, the distribution of differences is contained within ±1 m, except for depths of 10–12 m ($Bias$ = −1.16 m; Table 2 and Fig. 4), which is probably related to the inherent limitations of the bathymetric LiDAR dataset in water depths greater than 10 m resulting from the small number of depth points retrieved (N = 208; Fig. 3, Table 2). Maximum and minimum residuals within all depth classes correspond to depth points where the depth-retrieval linear algorithm was ineffective in providing accurate depth values. Class 1 (Fig. 4 and Table 2), which covers a depth range in which it is reasonable to expect significant morphological changes over a 2-year period, also had higher values of $Bias$ (0.61 m), $DifMedian$ (0.60 m), and $RMSE$ (0.94 m). It is also within this class that a lower accuracy of the depth-retrieval method is expected because of the stirring of suspended sediment and increased turbidity related to wave breaking. The $Bias$ decreases to values close to 0 for Class 2 ($Bias$ = 0.01 m, 2–4 m) and Class 3 ($Bias$ = −0.07 m, 4–6 m), increasing to −0.26 m for Class 4 (6–8 m) and −0.31 m for Class 5 (8–10 m) (Table 2 and Fig. 4). $Bias$ and $DifMedian$, the measures of precision, do not change much for Classes 1–4 but Class 5 presents a very low $DifMedian$ (−0.02 m) when compared with the $Bias$ (−0.31 m), which indicates that outliers affect the $Bias$ within this depth class more than in other classes (Table 2). The four classes comprising the depth range of 2–10 m (Classes 2 to 5) include 82% of the N sampled points (Fig. 4), whereas Class 1 contains 17% of the points. The spread in the data points can be evaluated by the variance (Var), which measures how far apart are the depth values retrieved using the linear algorithm from the corresponding LiDAR depths. Using all data except those in Class 6, which represents less than 1% of the dataset, the value of Var is ~0.50 m^2 for three depth classes (Classes 1, 3, and 4, 64% of the data points), ~0.70 m^2 (Class 2, 27% of the data points), and ~1.12 m^2 (Class 5, 9% of the data points) (Table 2). It is reasonable to assume that if outliers were removed and morphological variations neglected (inherent in nearshore dynamics for a 2-year period), the algorithm would be capable of retrieving depths within ±0.5 m of values acquired with LiDAR data for depths between 0 and 8 m. For the five shallowest depth classes (i.e., disregarding Class 6), the value of $RMSE$ ranges between 0.71 m (Class 3) and 1.10 m (Class 5), with a mean of 0.80 m.

4.2. Nearshore satellite-derived map

Fig. 5D, which masks data differences of <±0.5 m, shows that significant differences occur in the areas between profiles P1 and P2 and between P10 and P12, with the latter profiles being located in the area adjacent to the naturally migrating Ancão Inlet. The $Bias$ and $DifMedian$ for AoI1 are 0.01 m and 0.03 m, respectively, whereas Var and $RMSE$ are 0.56 m^2 and 0.75 m, respectively. For AoI2, the differences are not concentrated in particular parts but are distributed over the entire area in the deeper nearshore section (Fig. 8D). This behaviour was expected after analysing the spatial distribution of residuals in sector E in Fig. 3, where a reduction in the number of LiDAR data acquired for depths greater than 6 m can be observed. However, an exception to this, where LiDAR data for depths greater than 6 m were effectively acquired, includes the easternmost area of Tavira Island, adjacent to Tavira Inlet, that is, AoI2. For AoI2, the $Bias$ and $DifMedian$ are −0.69 m and −0.63 m, whereas Var and $RMSE$ are 0.90 m^2 and 1.17 m, respectively (Table 3).

The DMM grid generated for AoI2 (Fig. 8) reveals large areas where the SDB depths are shallower than the corresponding LiDAR depths, especially for depths greater than 6 m, which was not observed in the analysis of AoI1. This can be seen for all nine cross-shore profiles extracted for AoI2 (Fig. 9), in which the maximum SDB depths are close to 6 m, limiting the vectorisation of the SDB 8-m isobath (Fig. 10D). Inspection of the extracted nearshore profiles in both AoI1 (Fig. 6) and AoI2 (Fig. 9) reveals that the maximum deviation of the SDB in comparison with LiDAR data occurs between depths of 0 and 2 m (Table 2) and that variability in the depth range of 2 to 8 m is generally less than ±0.5 m. Regarding AoI1 (Fig. 6), two profiles (P1 and P11) show quite different behaviour between the SDB and both LiDAR (2- and 30-m resolution) extracted profiles. All the other profiles show the expected higher elevation differences between depths of 0 and 4 m, which are likely related to real morphological changes. This assumption seems to be confirmed by the close match between SDB extracted profiles and the LiDAR profiles for depths between 4 and 10 m. For AoI2, the agreement between SDB and both LiDAR extracted profiles is significantly better for depths from 0 to 6 m; however, the SDB profiles deviate significantly for the nearshore profile sections at depths greater than 6 m. As LiDAR data exist for depths greater than 6 m, the discordance appears to be related to the optical properties of the water and/or bottom properties that interfere directly with the retrieval of depth using the linear algorithm (i.e., a constant and/or incorrect DN on one or more Landsat 8 bands).

The 2-, 4-, 6-, and 8-m isobaths from the SDB extracted for both AoI1 (Fig. 7) and AoI2 (Fig. 10) were compared with their equivalent LiDAR (2- and 30-m resolution) isobaths and show a very consistent spatial behaviour. Major differences can be seen in the areas adjacent to tidal inlets for the 2-m (Fig. 7A) and 4-m (Fig. 7B) isobaths in AoI1, as well as for the 6-m isobath immediately downdrift of Tavira Inlet (Fig. 10C), and for the 8-m isobath (Fig. 10D) of AoI2. It was not possible to vectorise the 8-m isobath of AoI2 given the limitation on retrieving bathymetry for depths greater than 6 m in AoI2.

4.3. Validation of the depth-retrieval algorithm

The reliability of the depth-retrieval algorithm to produce SDB maps was assessed using a third independent data source, that is, dedicated small-scale echo-sounder bathymetries acquired in AoI3 and AoI4 (Fig. 5). SDB maps were produced using the determined coefficients (Eq. 6) on a new Landsat 8 scene (26 April 2013, Table 1). Given the similar timings of the surveys and the satellite image, in this comparison it is possible to assume negligible bathymetric change between the surveys and the date of the image. Because the same areas (AoI3 and AoI4) were surveyed and the XYZ data were interpolated using the same limits, method, and intervals, the DMM grid is (Figs 11C and 12C) used to compare the echo-sounding + RTK–DGPS map with the SDB map is expected to be a reliable indicator of the SDB method for retrieving shallow-water bathymetry. It also permits a direct comparison to be made of the SDB map with the results of conventional hydrographic methods, both geospatially and statistically, further allowing an assessment of the validity of using SDB maps for monitoring the dynamics of coastal sectors. In addition, a comparison of the LiDAR bathymetry and the echo-sounder data for AoI3 and AoI4 is provided in Figs 11D and 12D, respectively, to illustrate the degree of temporal change within a 2-year interval (i.e., LiDAR 06/2011 and echo-sounding 04/2013). Volumetric computations showing accretion/erosion morphodynamic variability are given in Table 3.

Figs 11C and 12C show the DMM grids between the echo-sounding + RTK–DGPS and the SDB maps for AoI3 and AoI4, respectively. The DMM grids are useful for locating the higher deviations and for identifying possible reasons for such deviations. Most of the differences occur in areas with depths of 0–2 m (Fig. 11C) or with depths of >8 m (Fig. 12C). In general, differences only rarely exceed ±1 m, and there are extensive areas with depths of 4–6 m where differences are less than ±0.25 m. The SDB maps (Figs 11B and 12B) are effective for representing the nearshore isobaths as well as the shapes of the bottom morphologies. The contour limits of the swash bar (Fig. 11B) and of the ebb delta (Fig 12B), both identified on the SDB maps, are clearly defined (as shown by the deflection of isobaths) when compared with the echo-sounding + RTK–

DGPS surveys (Figs 11A and 12A, respectively). This result is relevant because both surveys cover areas of complex environments: AoI3 is an area adjacent to a migrating inlet and AoI4 is situated in the vicinity of a stabilised inlet (Fig. 1). The results of the statistical analysis (Table 3) for AoI3 and AoI4 are similar: $Bias$ is 0.01 m, Var is 0.38–0.39, and both values of $RMSE$ are 0.62 m, with $DifMedian$ being the only parameter presenting a non-negligible difference (0.18 m and −0.07 m, respectively). Finally, Figs 11D and 12D present DMM grids to assess the degree of morphological change between the LiDAR and the SDB maps, given the time difference between the datasets (i.e., 2 years). The red/blue values in Figs 11D and 12D signify that accretion/erosion has occurred, respectively.

AoI3 is located adjacent to a migrating inlet (Ancão Inlet), and significant changes are likely to occur during a 2-year interval (the inlet migrates from west to east, with the direction of net alongshore transport being related to prevailing southwesterly conditions) (Fig. 11D). Such changes include accretion in the west while the barrier builds up over the former channel, forcing channel migration eastwards and causing erosion of the eastern adjacent barrier (the westernmost part of Barreta Island, Fig. 1). Those patterns are clearly observed in Fig. 11D with the formation of the swash bar updrift (red areas), the formation of two consecutive channels in the area located in the centre of the image, and general erosion in the shallow area between 0 and 2 m depth (blue areas).The total surveyed area recorded erosion of ~0.66 m^3/m^2 for the 2-year period (Table 3).

In AoI4, accretion is observed in the central area (inlet channel) and erosion in the western part of the survey area (where the ebb tidal delta is located). These observations are consistent with the recent evolution of the system, that is, the ebb delta is regularly dredged to counteract the sediment movement from the ebb delta towards the entrance channel through the delta terminal lobe. Overall, the total surveyed area recorded accretion of ~0.14 m^3/m^2 (Table 3) for the 2-year period, which is in agreement with the siltation tendency of this particular inlet, especially at the entrance channel. Excluding the ebb delta and the main channel, the elevation differences only rarely exceed ±1 m, with extensive areas where differences are less than ±0.25 m (Fig. 12D).

5. Discussion

Here, the determination of nearshore bathymetry, shoreline position, and accurate nearshore isobaths for different cases were examined by comparing SDB maps with data from different topographic/bathymetric surveying techniques (high- and medium-resolution LiDAR and RTK–DGPS + single-beam echo-sounder bathymetries). Bathymetric maps are conventionally represented by isobaths, which connect points of equal depth. The inner and offshore limits of several morphological features such as sand bars, deltas, and inlet channels can be both identified and spatially defined based on the configuration (including deflection) of isobath contours. The delineation of these morphological features is essential for performing volume computations and for estimating sediment paths and budgets within coastal cells. SDB nearshore profiles and isobaths retrieved for the selected areas of interest showed a very robust comparison with analogue determinations using both high- and medium-resolution LiDAR datasets. Discrepancies between SDB profiles and isobaths and LiDAR observations were noticeable only where prominent intertidal bars occur close to the inlets, as these are the areas where the most relevant morphological changes occur. It is also in these areas that the depth-retrieval algorithm records the worst results because the accuracy of the depth retrieval is limited by water turbidity caused by wave action, suspended sediment, and particulate matter, which limit the penetration of light (i.e., from both LiDAR and OLI sensors).

After assessing and calibrating the linear transform model, the coefficients of Eq. 6 were successfully used to derive SDB maps from another Landsat 8 image. Those maps were compared with independent bathymetric data acquired within the same time interval as the Landsat 8 image. The results presented confirmed the ability to use SDB maps to adequately identify nearshore isobaths, resolve nearshore bars, extract the nearshore profile, and delineate morphological features for areas with depths of <12 m in shallow coastal waters without significant wave breaking. The lower accuracy and precision of the SDB technique is considered to be related to the poor performance of the depth-retrieval linear algorithm for depths greater than 8 m. A possible explanation for this may be related to geographic and environmental controls, that is, the W and E sectors are exposed to different wave regimes, causing differences in optical conditions of the water (e.g., particles in suspension, chlorophyll-a, and bottom properties). Where the depth-retrieval linear algorithm is successful in extracting depths, the extracted values present higher residuals (areas adjacent to Tavira Inlet, Fig. 3 Class 5).

In this paper, a DOS method was applied to perform the atmospheric correction and a linear retrieval algorithm was applied using coefficients computed from a multiple linear regression performed with high-resolution LiDAR data. The adopted procedures are straightforward and are based on freely available images, and allowed shallow nearshore bathymetry to be represented well for depths less than 12 m. However, to improve the stability or robustness of the regressed model parameters over time, other Landsat 8 satellite images need to be analysed and compared with nearshore surveys. As an example, Brando et al. (2009) compared the accuracy of the depth-retrieval algorithm by comparison with acoustic depths at Rous Channel located in Moreton Bay (Australia) for depths of 0–30 m, with a 2-month interval between datasets. A greater agreement was found in shallow, clear water than in deeper or more turbid water near the coast (e.g., from 1–5 m depth, $Bias$ of 0.43 m, $DifMedian$ of 0.42 m, and $RMSE$ of 1.35 m). Brando et al. (2009) optimised the inversion algorithm by comparing the measurable remote sensing reflectance from the image with a modelled reflectance. The procedure adopted by Brando et al. (2009) allowed differences related to environmental variables such as water column depth, substrate composition, and the concentration of optical active constituents on the water column (chlorophyll-a, the concentration of dissolved organic matter, and non-algal particles) to be minimised, as well the range of the technique to be extended.

In general, SDB retrieved from Landsat 8 images presents a new perspective for remotely sensed bathymetry extraction and can be used to complement data from survey sources such as single-beam echo-sounder data, which are normally obtained at medium (profiling interval 25–30 m) to coarse (>30 m) resolution. This implies that SDB can effectively deliver data to complement such surveys and provide a similar spatial representation of nearshore variability. In particular, the ability to extract depth contours from satellite-derived bathymetry can be a straightforward and accessible method for evaluating morphological changes in the nearshore. This method has high potential for acquiring cost-effective, long-term time-series of coastal morphology over extensive areas and at the same time provides high-frequency data (i.e., approximately fortnightly intervals, 16 days). The medium-resolution maps derived from the presented method can be used to improve the prediction of hydro-morphodynamic modelling simulations such as those given by X-Beach (Roelvink et al., 2009) by allowing the continuous extraction of model input morphodynamic parameters (e.g., submerged beach slope).

6. Conclusion

An improved understanding of coastal zone evolution and processes is based partially on the existence of detailed and reasonably accurate monitoring datasets. Such datasets have become fundamental for coastal research, modelling, and management. The present contribution assessed the potential of satellite-derived bathymetry (SDB) maps for providing nearshore bathymetry at medium resolution from freely available Landsat 8 imagery, and revealed the value of the approach for the monitoring and management of coastal morphological evolution. The results showed that bathymetry obtained from multi-spectral satellite data is more accurate for shallow water depths (0 to 8 m) than for greater depths (8–12 m), a limitation inherent in a passive optical detection system; however, in the Ria Formosa case study, the decrease in accuracy with depth was also a function of the more limited availability of the LiDAR data used to tune the image-to-depth conversion algorithm at greater depths. The SDB maps were able to provide good approximations of the shoreline position and nearshore isobath contours for different cases along a highly complex coastline that includes morphological features such as barrier islands, inlets, ebb deltas, and alongshore and swash bars. In all instances, the extracted morphological features (i.e., nearshore isobaths and profiles) displayed reasonable accuracy when compared with those derived from traditional monitoring methods.

Improved satellite imagery collection, processing algorithms, and workflows make SDB a real and useful survey solution for monitoring coastal areas and for producing rapidly deliverable digital bathymetric models. Although SDB has great potential in its current state, the good quality of the results presented here for the 60-km stretch of coast of the Ria Formosa area is inherently related to the availability of the high-frequency LiDAR data that were used to perform the regression to obtain the coefficients of Lyzenga's (1978, 1985) model. In other words, if no in situ water depths are available and/or depth measurements are sparse, then the model cannot be applied with the same degree of rigor. However, SDB has the potential to complement traditional but expensive maritime charting techniques such as acoustic and LiDAR surveys, because the method does not need devoted boats, aircraft, or other survey systems. Depending on weather conditions and satellite orbit timings, the surveys can be performed on a regular basis, giving the potential to create historical datasets from imaging archives. If the robustness of the coefficients is further analysed, the technique can be used to derive nearshore bathymetric maps to assist with coastal monitoring. Finally, the accuracy of SDB maps is partly a function of water clarity, depth, and wave climate. Better approximations could be derived by using algorithms that correct for environmental variables such as the concentration of optically active constituents in the water column (e.g., chlorophyll-a, organic dissolved matter, and suspended sediment). With respect to wave climate, the method presented here works better for calm conditions, and major deviations in the accuracy of depth assessments occur in the breaking zone.

Acknowledgments

André Pacheco and Carlos Loureiro were supported by the Portuguese Foundation for Science and Technology (grant numbers SFRH/BPD/76110/2011 and SFRH/BPD/85335/2012). AoI3 bathymetric data were acquired under project RUSH (from RUn up to overwaSH) (PTDC/CTE-GIX/116814/2010) funded by the Portuguese Foundation for Science and Technology. The authors acknowledge the anonymous reviewers, whose comments helped to greatly improve an earlier version of this manuscript.

List of Acronyms

AoI	Area of Interest
DEM	Digital Elevation Model
DMM	Difference Map Method
DOS	Dark Subtraction Object
LiDAR	Light Detecting and Ranging
NIR	Near Infrared Band
OLI	Operational Land Imagery
SDB	Satellite-Derived Bathymetry

SNR	Signal to Noise Ratio
TIRS	Thermal Infrared Sensor

List of Symbols

$a(\lambda)$	Absorption coefficient
$b_b(\lambda)$	Backscatter coefficient
d_b	Bottom depth
DN	Digital number
d	Earth–Sun distance
E_d	Downwelling irradiance
E_o	Solar constant
$E_{sum\lambda_i}$	Exo-atmospheric solar irradiance from band λ_i
H_s	Significant wave height
θ_0	Solar zenith angle
θ_v	Sub-surface viewing angle from nadir
θ_w	Sub-surface solar zenith angle
L_T	Total radiance (measured by the satellite)
L_w	Water-leaving radiance
$L_{1\%}$	Minimum scatter radiance
R	Irradiance reflectance
R_b	Bottom albedo
R_r	Rayleight reflectance
R_{rs}	Remote sensing reflectance
R_T	Total reflectance
R_w	Reflectance of water
R_∞	Water reflectance (if optically deep)

TOA Top of Atmosphere Reflectance

T_0 Transmission coefficient Sun-to-Earth

T_1 Transmission coefficient Earth-to-Sun

Z_{LiDAR} Depth acquired with LiDAR

Z_{LSAT8} Satellite-derived depth

φ Viewing azimuth angle from solar plane

References

Albert, A., Gege, P., 2006. Inversion of irradiance and remote sensing reflectance in shallow water between 400 and 800 nm for calculation of water and bottom properties. Applied Optics 45: 2331–2343.

Albert, A., Mobley, C.D., 2003. An analytical model for subsurface irradiance and remote sensing reflectance in deep and shallow case-2 waters. *Opt. Express* 11: 2873–2890.

Brando, V., Anstee, J.M., Wettle, M., Dekker, A.G., Phinn, S.R., Roelsema, C., 2009. A physical based retrieval and quality assessment of bathymetry from suboptimal hyperspectral data. *Remote Sens. Environ.*113: 755–790.

Chavez, P.S., Jr. 1988. An improved dark-object subtraction technique for atmospheric scattering correction of multispectral data. *Remote Sens. Environ.* 24: 459–479.

Chavez, P.S., Jr. 1996. Image-based atmospheric corrections–revisited and improved. Photogramm. *Eng. Remote Sensing* 62(9): 1025–1036.

Costa M., Silva R., Vitorino J., 2001. Contribuição para o estudo do clima de agitação marítima na costa Portuguesa. 2as Jornadas Portuguesas de Engenharia Costeira e Portuária in CD-ROM. (in Portuguese).

Dekker A.G., Phinn, S.R., Anstee J., Bissett, P., Brando V., Casey, B., Fearns, P., Hedley, J., Klonowski, W., Lee, Z.P., Lynch, M., Lyons, M., Mobley, C., Roelfsema, C. 2011. Intercomparison of shallow water bathymetry, hydro-optics, and benthos mapping techniques in Australian and Caribbean coastal environments. *Limnol. Oceanogr. Methods* 9: 396–425.

Hicks D.M., Hume T.M., 1997. Determining sand volumes and bathymetric change on an ebb-tidal delta. *J. Coast. Res.* 13 (2): 407–416.

Horta, J., Pacheco, A., Moura, D., Ferreira, Ó., 2014. Can recreational Echosounder-Chartplotter systems be used to perform accurate nearshore bathymetric surveys? *Ocean Dyn.* 64:1555–1567.

IHO, 2008. International Hydrographic Organization Standards S-44 for Hydrographic Surveys, Special Publication No 44, 28 pp.

Keith, D.J., Shaeffer, B.A., Lunetta, R.S., Gould, R.W., Rocha, K., Cobb, D.J. 2014. Remote sensing of selected water-quality indicators with the hyperspectral imager for the coastal ocean (HICO) sensor. *Int. J. Remote Sens.*35(9): 2927–2962.

Lyzenga, D.R. 1978. Passive remote sensing techniques for mapping water depth and bottom features. *Apll. Opt.* 17: 379–383.

Lyzenga, D.R. 1985. Shallow-water bathymetry using combined LiDAR and passive multispectral scanner data. *Int. J. Remote Sens.* 6: 115–125.

Mobley, C.D., Sundman L.K., Davis, C.O., Downes, T.V., Leathers, R.A, Montes M.J., Bissett W.P., Kohler D.D., Reid R.P., Louchard E.M., Gleason A., 2005. Interpretation of hyperspectral remote-sensing imagery via spectrum matching and look-up tables. *Apll. Opt.* 44:3576–3592.

Nazeer, M., Nichols, J.E., Yung, Y. 2014. Evaluation of atmospheric correction models and Landsat surface reflectance product in an urban coastal environment. *Int. J. Remote Sens.* 35(16): 6671–6291.

Pacheco, A., Williams, J.J., Ferreira, Ó., Garel, E., Reynolds, S., 2011. Application of Sediment Transport Models to a Multiple-Inlet System. *Estuar. Coast. Shelf Sci.* 95: 119–134.

Pawlowicz, R., Beardsley, B., Lentz, S., 2002. Classical tidal harmonic analysis including error estimates in MATLAB using T_TIDE. *Comput. Geosci.* 28: 929–937.

Roelvink, D., Reniers, A., van Dongerenb, A., de Vries, J., McCall, R., Lescinski, J., 2009. Modelling storm impacts on beaches, dunes and barrier islands. *Coastal Eng.* 56(11–12): 1133–1152.

Roy, D.P., Wulder, M.A., Loveland, T.R., Woodcock, C.E., Allen, R.G., Anderson, M.C., Helder, D., Irons, J.R., Johnson, D.M., Kennedy, R., Scambos, T.A., Schaaf, C.B., Schott, J.R., Sheng, Y., Vermote, E.F., Belward, A.S., Bindschadler, R., Cohen, W.B., Gao, F., Hipple, J.D., Hostert, P., Huntington, J., Justice, C.O., Kilic, A., Kovalskyy, V., Lee, Z.P., Lymburner, L., Masek, J.G., McCorkel, J., Shuai, Y., Trezza, R., Vogelmann, J., Wynne, R.H., Zhu, Z. 2014. Landsat-8: Science and product vision for terrestrial global change research. *Remote Sens. Environ.*145: 154–172.

Stauble D. 1998. Techniques for measuring and analysing inlet ebb shoal evolution. *Coast. Eng. Techn. Note* IV(13), 12 pp.

Stumpf, R.P, Holderied, K., Sinclair, M., 2003. Determination of water depth with high resolution satellite imagery over variable bottom types. *Limnol. Oceanogr.* 48 (I/ 2): 547–556.

Table Captions

Table 1. Details of the datasets used in the present study (LiDAR, Landsat 8 scenes, and echo-sounder + RTK–DGPS). XY is referenced to WGS84 UTM ZONE 29 and Z to mean sea level (MSL).

Table 2. Constant coefficients derived from the multiple linear regression between water reflectance band and LiDAR depth. Residual statistics between the satellite-derived depth (Z_{LSat8}) and (Z_{Li}) and LiDAR depth for different depth classes.

Table 3. AoI1 univariate statistics obtained by comparing Bm2 and Bm3. AoI2 univariate statistics obtained by comparing Bm2 and Bm3. AoI3 and AoI4 univariate statistics obtained by comparing the echo-sounding + RTK–DGPS survey performed in late April 2013 with the SDB maps produced using the Landsat 8 scene from 26 April 2013.

Figure Captions

Figure 1. (A) Ria Formosa multi-inlet system (southern Portugal). Areas of Interest AoI1 and AoI3 (B) and AoI2 and AoI4 (C) are represented by aerial photography images to a depth limit of ~12 m.

Figure 2. Workflow processing steps for deriving SDB maps from Landsat 8 images (DN: Digital number; L_T: Total radiance; $L_{1\%}$: Minimum scatter radiance; R_w: Reflectance of water; R_T: Total reflectance; R_∞: Water reflectance; X_i, X_j, and X_k are from Lyzenga's (1978, 1985) linear solution for albedo correction; a_0, a_i, a_j, and a_k are constants determined by multiple linear regression; Z_{LiDAR}: Depth acquired with LiDAR; Z_{LSAT8}: Satellite-derived depth.

Figure 3. Spatial distribution of the residual between Z_{LSat8} and Z_{LiDAR} along X coordinate WGS84 UTM29 for different depth classes. Vertical grey bands represent the inlet areas. Horizontal dark-grey bands represent residuals less than 2 m. The smaller amount of data at greater depths results from LiDAR data limitations (see main text Section 3.2.).

Figure 4. Histogram of differences between satellite-derived depth (Z_{LSat8}) and LiDAR depth (Z_{LiDAR}) by depth class.

Figure 5. (A) AoI1 bathymetry contour map (Bm1) using the 2-m resolution 2011 LiDAR data superimposed with an aerial photograph of AoI1. (B) Bathymetry contour map (Bm2) with a 30-m resolution using 2011 LiDAR data resampling. (C) Satellite-derived bathymetry contour map (Bm3) with a 30-m resolution. (D) Difference map between Bm2 and Bm3. P1 to P12 represent the locations of the profiles extracted from bathymetric maps Bm1 and Bm2.

Figure 6. AoI1 nearshore cross-profiles spaced by 1000 m and extracted from bathymetric contour maps Bm1, Bm2, and Bm3.

Figure 7. (A) 2-m, (B) 4-m, (C) 6-m, and (D) 8-m isobaths extracted from Bm1 (LiDAR 2 m), Bm2 (LiDAR 30 m), and Bm3 (SDB 30 m) for AoI1. XY coordinates are referred to WGS84 UTM29 and Z contour lines to MSL.

Figure 8. (A) AoI2 bathymetry contour map (Bm1) using the 2-m resolution 2011 LiDAR data superimposed with an aerial photograph of AoI2. (B) Bathymetry contour map (Bm2) with a 30-m resolution using 2011 LiDAR data resampling. (C) Satellite-derived bathymetry contour map (Bm3), also showing AoI3. (D) Difference map between Bm2 and Bm3. P1 to P9 represent the locations of the profiles extracted from bathymetric maps Bm1, Bm2, and Bm3.

Figure 9. AoI2 nearshore cross-profiles spaced by 1000 m and extracted from bathymetric contour maps Bm1, Bm2, and Bm3.

Figure 10. (A) 2-m, (B) 4-m, (C) 6-m, and (D) 8-m isobaths extracted from Bm1 (LiDAR 2m), Bm2 (LiDAR 30 m), and Bm3 (SDB 30 m) for AoI2. XY coordinates are referred to WGS84 UTM29 and Z contour lines to MSL.

Figure 11. (A) AoI3 bathymetry contour map acquired using an echo-sounder synchronised with a RTK–DGPS in the area adjacent to Ancão Inlet on 26 April 2013. (B) Satellite-derived bathymetry (SDB) contour map (Bm3) with a 30-m resolution. (C) Difference map between A and B. (D) Difference map between LiDAR 05/2011 and SDB data derived from the Landsat 8 image of 26 April 2013; the red/blue values signify that accretion/erosion has occurred, respectively.

Figure 12. (A) AoI4 bathymetry contour map acquired using an echo-sounder synchronised with a RTK–DGPS in and around Tavira Inlet on 30 April 2013. (B) Satellite-derived bathymetry (SDB) contour map (Bm3) with a 30-m resolution. (C) Difference map between A and B. (D) Difference map between LiDAR 05/2011 and SDB data derived from the Landsat 8 image of 26 April 2013; the red/blue values signify that accretion/erosion has occurred, respectively.

Table 1. Details of the datasets used in the present study (LiDAR, Landsat 8 scenes, and echo-sounder + RTK–DGPS). XY is referenced to WGS84 UTM ZONE 29 and Z to mean sea level (MSL)

Dataset	Details and coverage	Type/Resolution
LiDAR	Topographic LiDAR LeicaALS60 Bathymetric LiDAR HawkEyeII Coverage: Portugal, to 8–10 m depth Datum: WGS84; Ellipsoid: WGS84 UTM Zone: 29; Z referred to MSL Date acquired= 2011-05	Combined model (topographic plus bathymetric LiDAR): Resolution 2 m Order 1A International Hydrographic Organisation Standards 44 (2008)
Landsat 8	Scene: LC82030342013164LGN00 Map projection: UTM Datum: WGS84; Ellipsoid: WGS84 UTM Zone: 29 Coverage: X: 494400–720900 Y: 4037100–4258200 Date acquired: 2013-06-13	8 Bands Digital Numbers (DNs) each 30 m Image attributes Min/Max Radiance Min/Max Reflectance Min/Max Pixel Value Radiometric Rescaling TIRS Thermal Constants Projection Parameters All in the *.MTL file provided by United States Geological Service
	Scene: LC82030342013116LGN01 Map projection: UTM Datum: WGS84; Ellipsoid: WGS84 UTM Zone: 29 Coverage: X: 494400–720900 Y: 4037100–4258200 Date acquired: 2013-04-26	
Echo-Sounder + RTK–DGPS	Sounding: Echotrac CV 100 Frequency: 200 kHz Positioning: RTK–DGPS TrimbleR6/5800 GPS Satellite signals: L1C/A, L1C, L2C, L2E, L5. Datum: WGS84; Ellipsoid: WGS84 UTM Zone: 29; Z referred to MSL Coverage: AoI3 Barreta Island AoI4 Tavira Inlet Date acquired 2013-04-26 (AoI3) 2013-04-30 (AoI4)	1 Hz data Resolution 25 m (single-beam echo-sounder lines run parallel at pre-planned line spacing); Bathymetry tide corrected (RTK) Echo-sounding accuracy: 0.01 m ±0.1% of depth Positioning performance for RTK surveying: Horizontal: 8 mm + 1 ppm RMS Vertical: 15 mm + 1 ppm RMS

Table 2. Constant coefficients derived from the multiple linear regression between water reflectance band and LiDAR depth. Residual statistics between the satellite-derived depth (Z_{LSat8}) and (Z_{Li}) and LiDAR depth for different depth classes

Multiple Linear Regression

$$\boldsymbol{Z_{LSat8} = a_0 + a_i(X_i) + a_j(X_j) + a_K(X_K)}$$

$R^2 = 0.88$, N = 35247 $\boldsymbol{a_0} = -2.39$; $\boldsymbol{a_i} = -6.05$; $\boldsymbol{a_j} = -0.33$; $\boldsymbol{a_k} = 8.25$

Residual statistics ($\boldsymbol{Z_{LSat8}\_Z_{LiDAR}}$)

	Depth Class (m)						
	Class 1 [0–2]	**Class 2 [2–4]**	**Class 3 [4–6]**	**Class 4 [6–8]**	**Class 5 [8–10]**	**Class 6 [10–12]**	**Overall [0–12]**
N	6145	9619	8377	7640	3258	208	35247
Bias (m)	0.61	0.01	−0.07	−0.26	−0.31	−1.16	−0.20
Std (m)	0.71	0.84	0.71	0.71	1.06	1.28	0.89
Var (m^2)	0.51	0.70	0.50	0.50	1.12	1.63	0.83
DifMedian (m)	0.60	0.05	−0.07	−0.37	−0.02	−0.77	−0.10
RMSE (m)	0.94	0.84	0.71	0.75	1.10	1.72	1.01
Max (m)	6.06	3.43	2.83	3.65	2.75	0.73	n/a
Min (m)	−2.03	−3.34	−3.72	−3.97	−3.54	−4.79	n/a

Table 3. AoI1 univariate statistics obtained by comparing Bm2 and Bm3. AoI2 univariate statistics obtained by comparing Bm2 and Bm3. AoI3 and AoI4 univariate statistics obtained by comparing the echo-sounding + RTK–DGPS survey performed in late April 2013 with the SDB maps produced using the Landsat 8 scene from 26 April 2013

AoI1	**Bathymetric Contour Map**	
	Bm2 (LiDAR 30 m)	**Bm3 (SDB 30 m)**
Mean (Z) (m)	−5.93	−5.94
Median (Z) (m)	−6.12	−6.41
Min (Z) (m)	−10.39	−10.77
Max (Z) (m)	−0.09	−0.46
Std (Z) (m)	2.62	2.84
$\boldsymbol{Var\ (\hat{z})}$	**0.56**	
$\boldsymbol{Bias(\hat{z}, z)}$	**0.01**	
$\boldsymbol{DifMedian(\hat{z}, z)}$	**0.03**	
$\boldsymbol{RMSE(\hat{z})}$	**0.75**	

AoI2	**Bathymetric Contour Map**	
	Bm2 (LiDAR 30 m)	**Bm3 (SDB 30 m)**
Mean (Z) (m)	−5.38	−4.69
Median (Z) (m)	−6.25	−5.64
Min (Z) (m)	−10.24	−7.38
Max (Z) (m)	−0.01	−0.52
Std (Z) (m)	2.74	2.00
$\boldsymbol{Var\ (\hat{z})}$	**0.90**	
$\boldsymbol{Bias(\hat{z}, z)}$	**−0.69**	
$\boldsymbol{DifMedian(\hat{z}, z)}$	**−0.63**	
$\boldsymbol{RMSE(\hat{z})}$	**1.17**	

AoI3	**Bathymetric Contour Map**	
	Echo-Sounder + RTK–DGPS	**SDB 30 m**
Mean (Z) (m)	−4.43	−4.44
Median (Z) (m)	−4.42	−4.72
Min (Z) (m)	−8.32	−7.97
Max (Z) (m)	−0.68	−0.13
Std (Z) (m)	1.75	2.21
$\boldsymbol{Var\ (\hat{z})}$	**0.39**	
$\boldsymbol{Bias(\hat{z}, z)}$	**0.01**	
$\boldsymbol{DifMedian(\hat{z}, z)}$	**0.18**	
$\boldsymbol{RMSE(\hat{z})}$	**0.62**	

AoI4	**Bathymetric Contour Map**	
	Echo-Sounder + RTK–DGPS	**SDB 30 m**
Mean (Z) (m)	−5.75	−5.53
Median (Z) (m)	−6.23	−5.93
Min (Z) (m)	−8.67	−6.90
Max (Z) (m)	−1.67	−0.74
Std (Z) (m)	1.44	1.28
$\boldsymbol{Var\ (\hat{z})}$	**0.38**	
$\boldsymbol{Bias(\hat{z}, z)}$	**0.01**	
$\boldsymbol{DifMedian(\hat{z}, z)}$	**−0.07**	
$\boldsymbol{RMSE(\hat{z})}$	**0.62**	

778 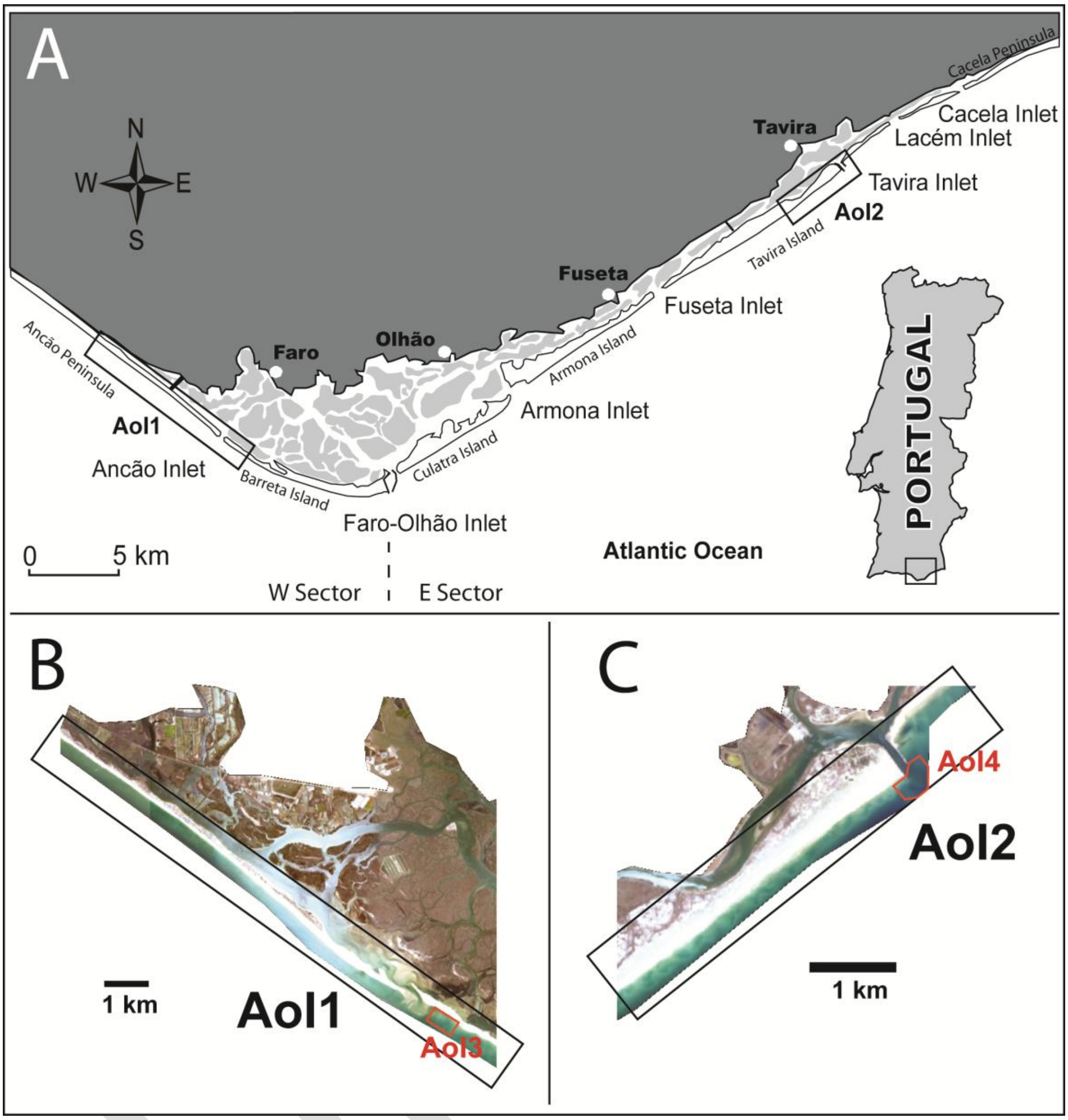

779 **Figure 1.** (A) Ria Formosa multi-inlet system (southern Portugal). Areas of Interest AoI1 and AoI3 (B)
780 and AoI2 and AoI4 (C) are represented by aerial photography images to a depth limit of ~12 m.

781

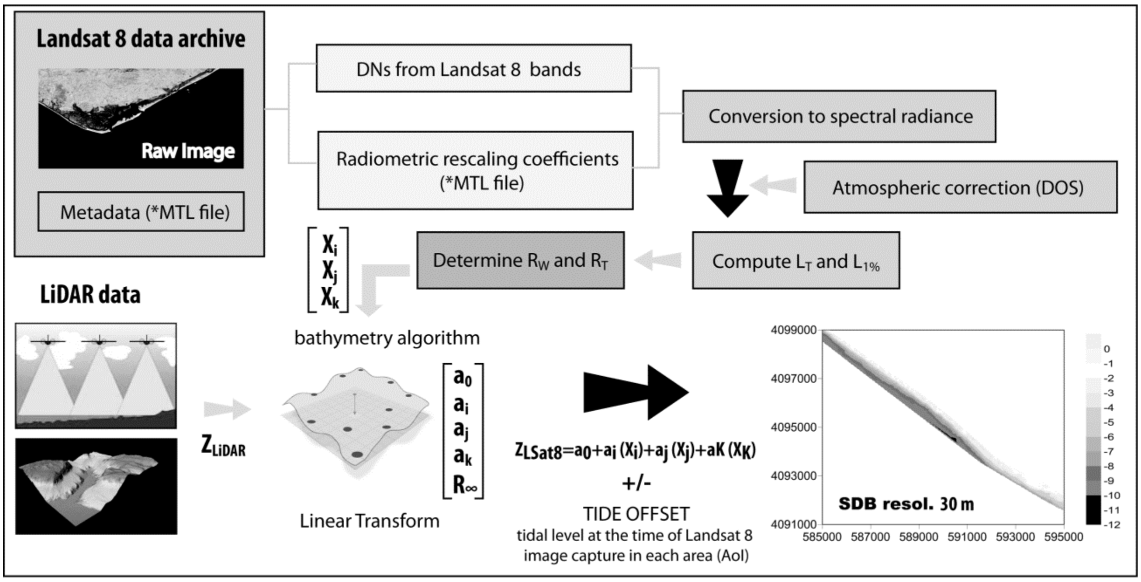

Figure 2. Workflow processing steps for deriving SDB maps from Landsat 8 images (DN: Digital number; L_T: Total radiance; $L_{1\%}$: Minimum scatter radiance; R_w: Reflectance of water; R_T: Total reflectance; R_∞: Water reflectance; X_i, X_j, and X_k are from Lyzenga's (1978, 1985) linear solution for albedo correction; a_0, a_i, a_j, and a_k are constants determined by multiple linear regression; Z_{LiDAR}: Depth acquired with LiDAR; Z_{LSAT8}: Satellite-derived depth.

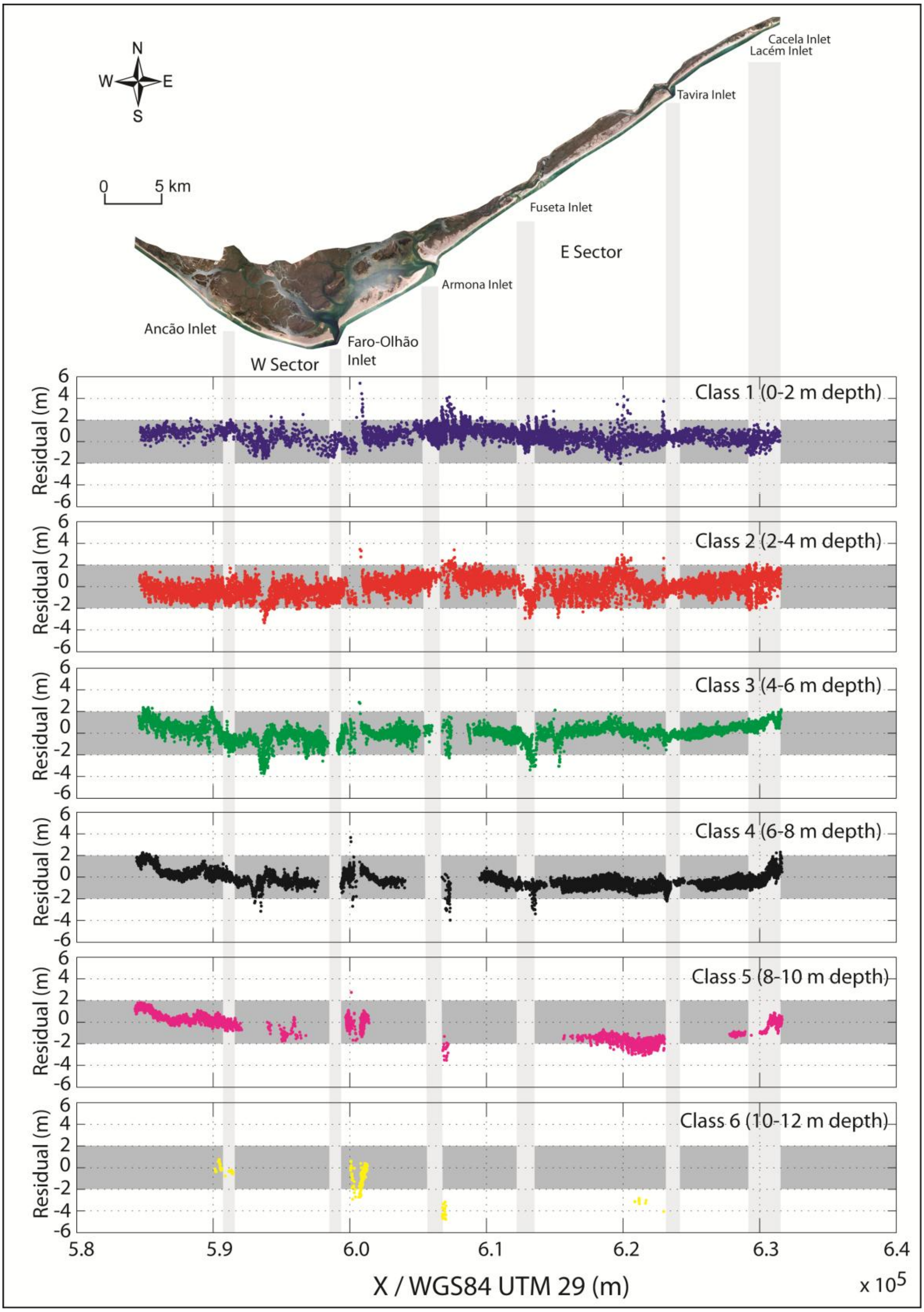

Figure 3. Spatial distribution of the residual between Z_{LSat8} and Z_{LiDAR} along X coordinate WGS84 UTM29 for different depth classes. Vertical grey bands represent the inlet areas. Horizontal dark-grey bands represent residuals less than 2 m. The smaller amount of data at greater depths results from LiDAR data limitations (see main text Section 3.2.).

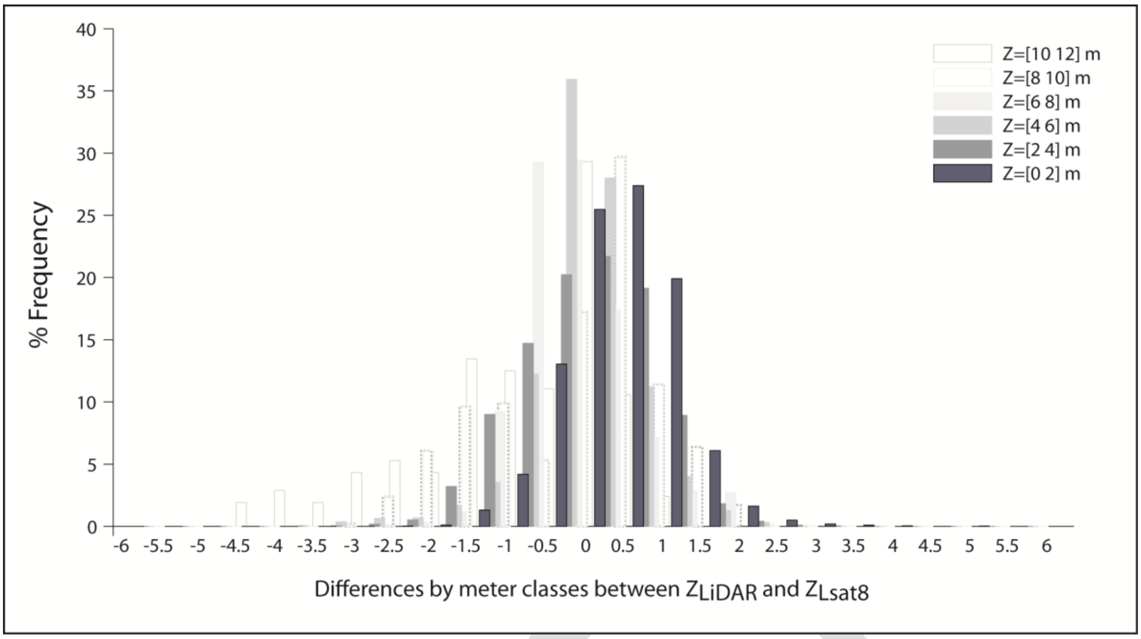

Figure 4. Histogram of differences between satellite-derived depth (Z_{LSat8}) and LiDAR depth (Z_{LiDAR}) by depth class.

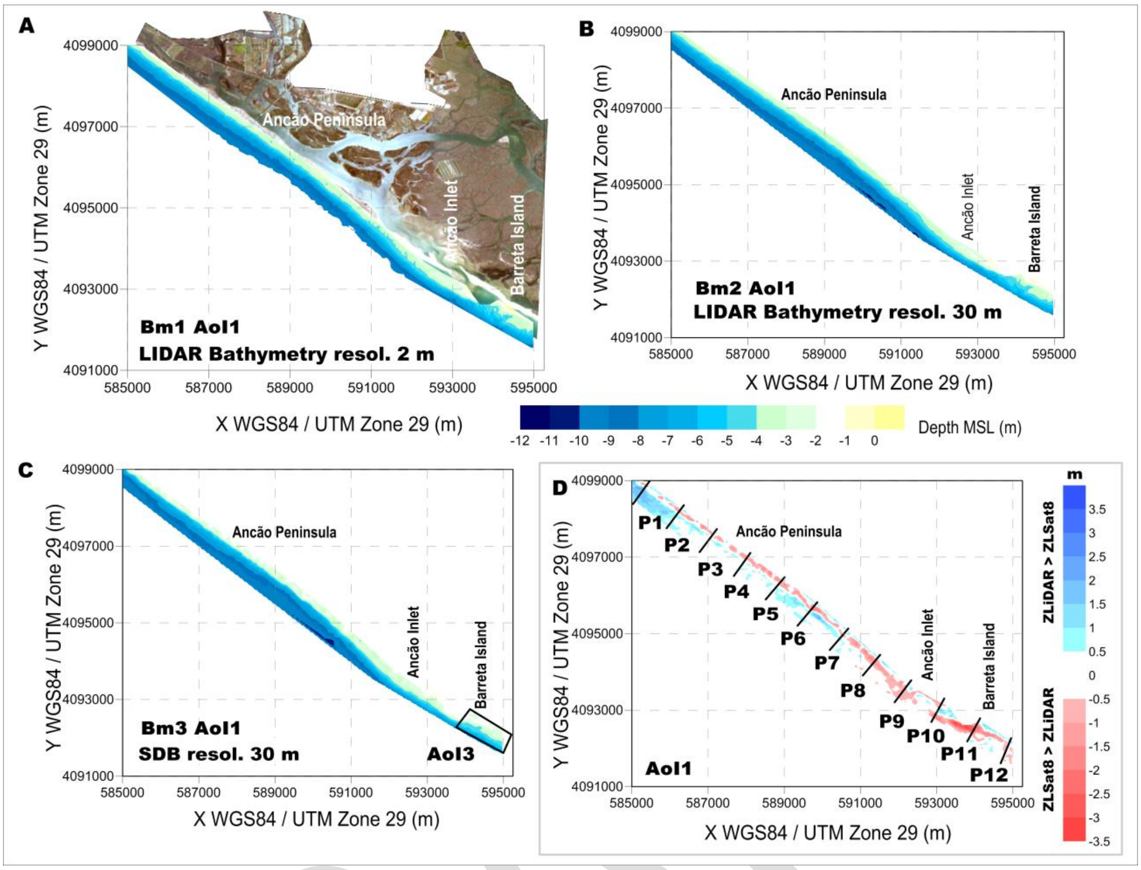

Figure 5. (A) AoI1 bathymetry contour map (Bm1) using the 2-m resolution 2011 LiDAR data superimposed with an aerial photograph of AoI1. (B) Bathymetry contour map (Bm2) with a 30-m resolution using 2011 LiDAR data resampling. (C) Satellite-derived bathymetry contour map (Bm3) with a 30-m resolution. (D) Difference map between Bm2 and Bm3. P1 to P12 represent the locations of the profiles extracted from bathymetric maps Bm1 and Bm2.

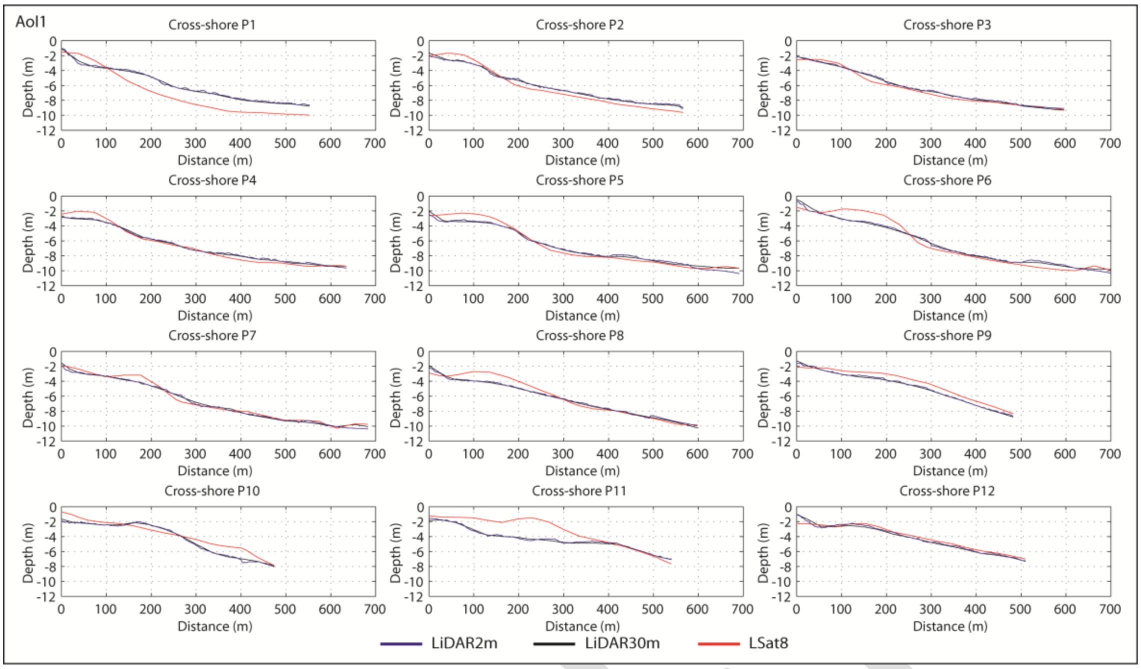

Figure 6. AoI1 nearshore cross-profiles spaced by 1000 m and extracted from bathymetric contour maps Bm1, Bm2, and Bm3.

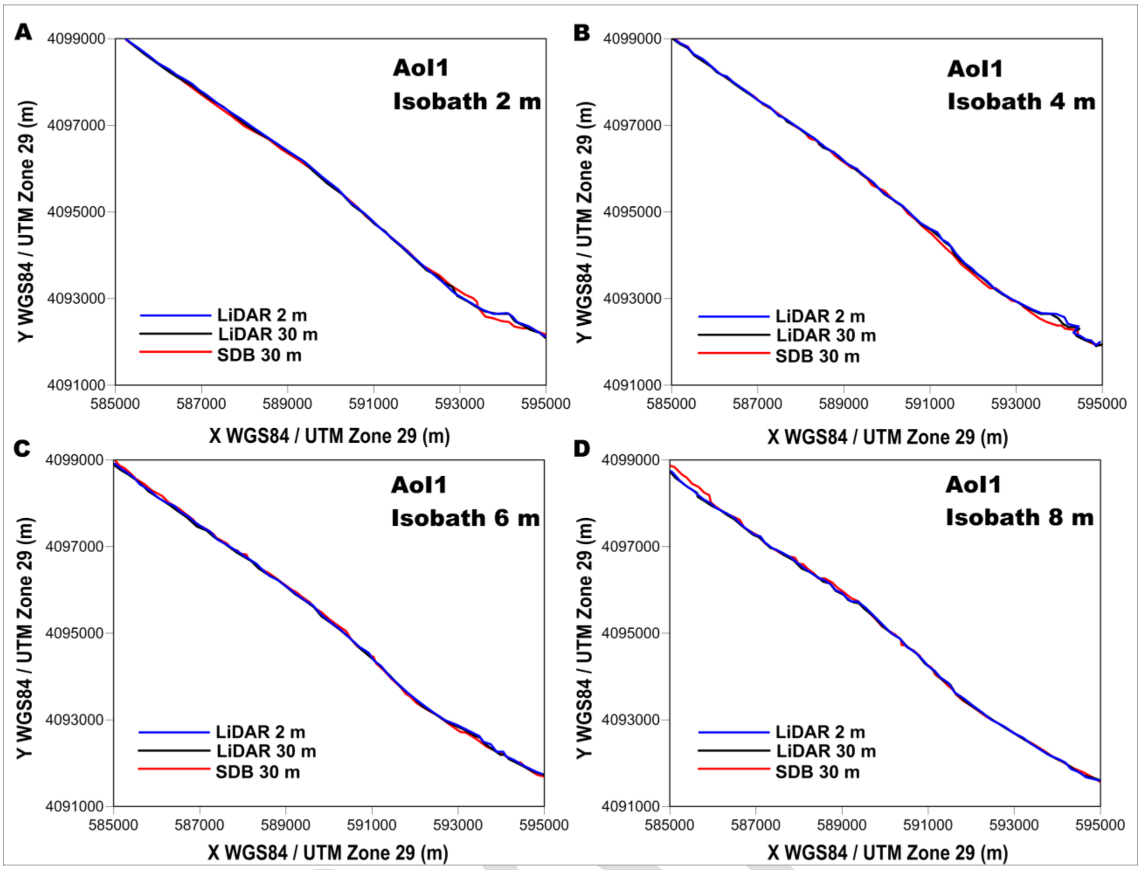

Figure 7. (A) 2-m, (B) 4-m, (C) 6-m, and (D) 8-m isobaths extracted from Bm1 (LiDAR 2 m), Bm2 (LiDAR 30 m), and Bm3 (SDB 30 m) for AoI1. XY coordinates are referred to WGS84 UTM29 and Z contour lines to MSL.

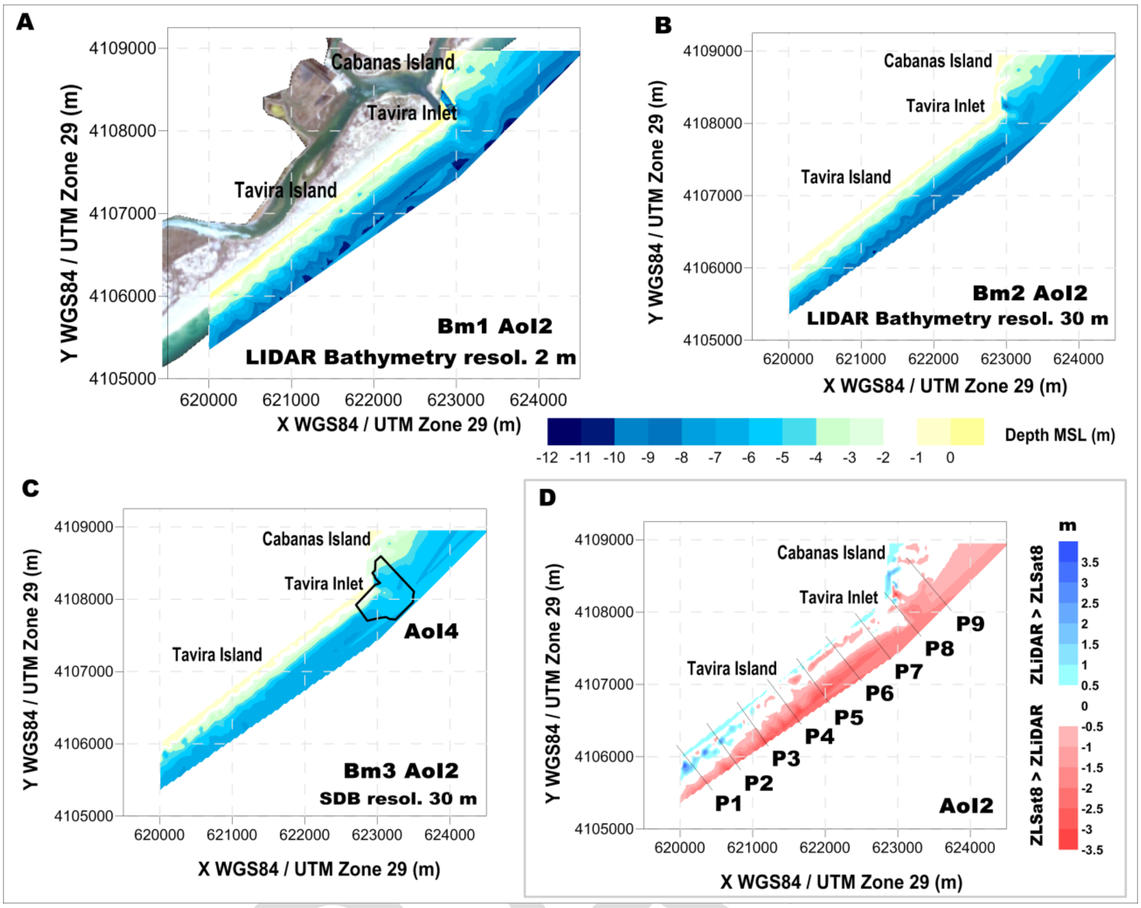

Figure 8. (A) AoI2 bathymetry contour map (Bm1) using the 2-m resolution 2011 LiDAR data superimposed with an aerial photograph of AoI2. (B) Bathymetry contour map (Bm2) with a 30-m resolution using 2011 LiDAR data resampling. (C) Satellite-derived bathymetry contour map (Bm3), also showing AoI3. (D) Difference map between Bm2 and Bm3. P1 to P9 represent the locations of the profiles extracted from bathymetric maps Bm1, Bm2, and Bm3.

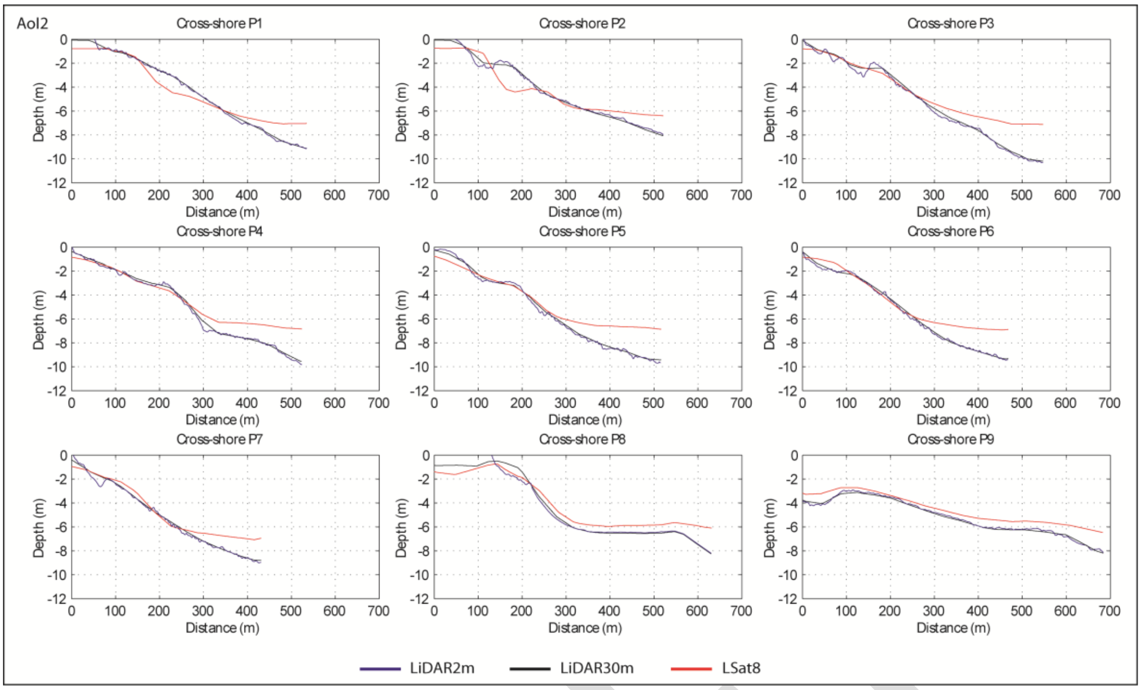

Figure 9. AoI2 nearshore cross-profiles spaced by 1000 m and extracted from bathymetric contour maps Bm1, Bm2, and Bm3.

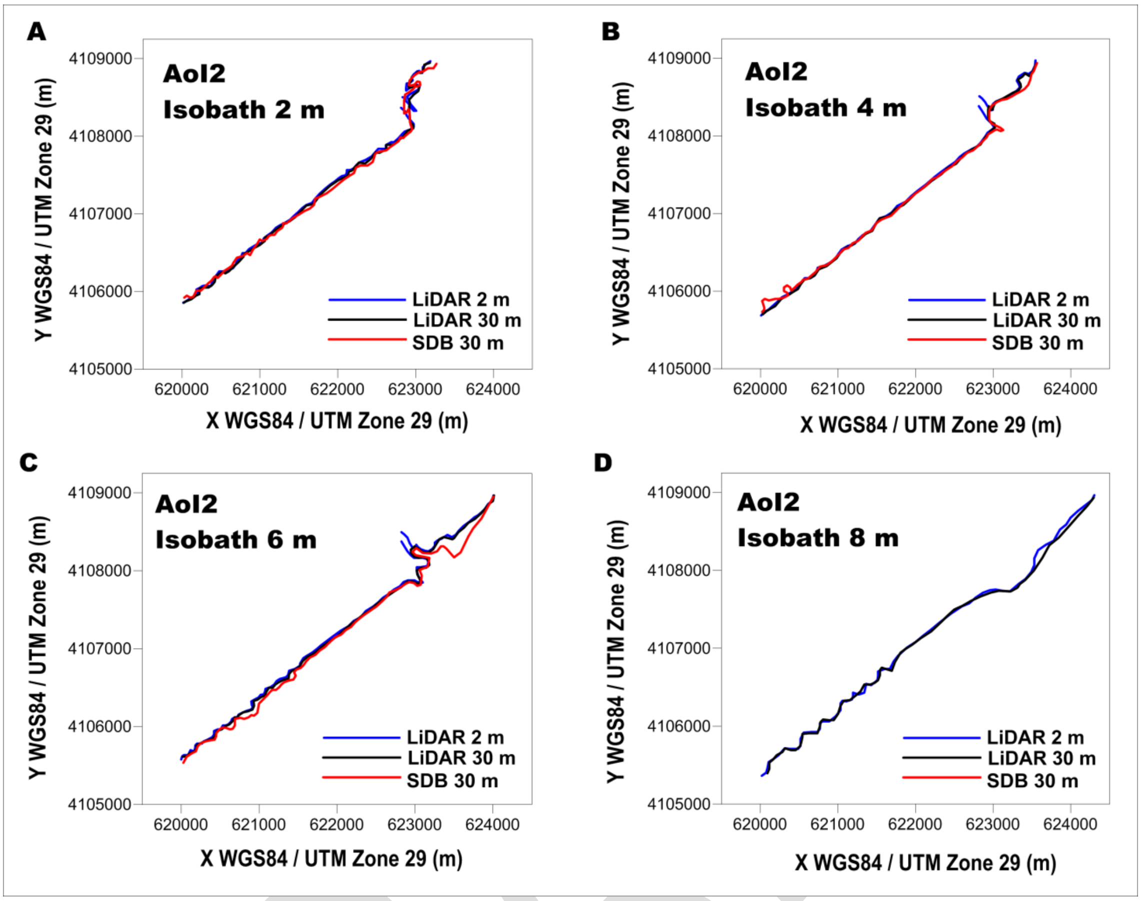

Figure 10. (A) 2-m, (B) 4-m, (C) 6-m, and (D) 8-m isobaths extracted from Bm1 (LiDAR 2m), Bm2 (LiDAR 30 m), and Bm3 (SDB 30 m) for AoI2. XY coordinates are referred to WGS84 UTM29 and Z contour lines to MSL.

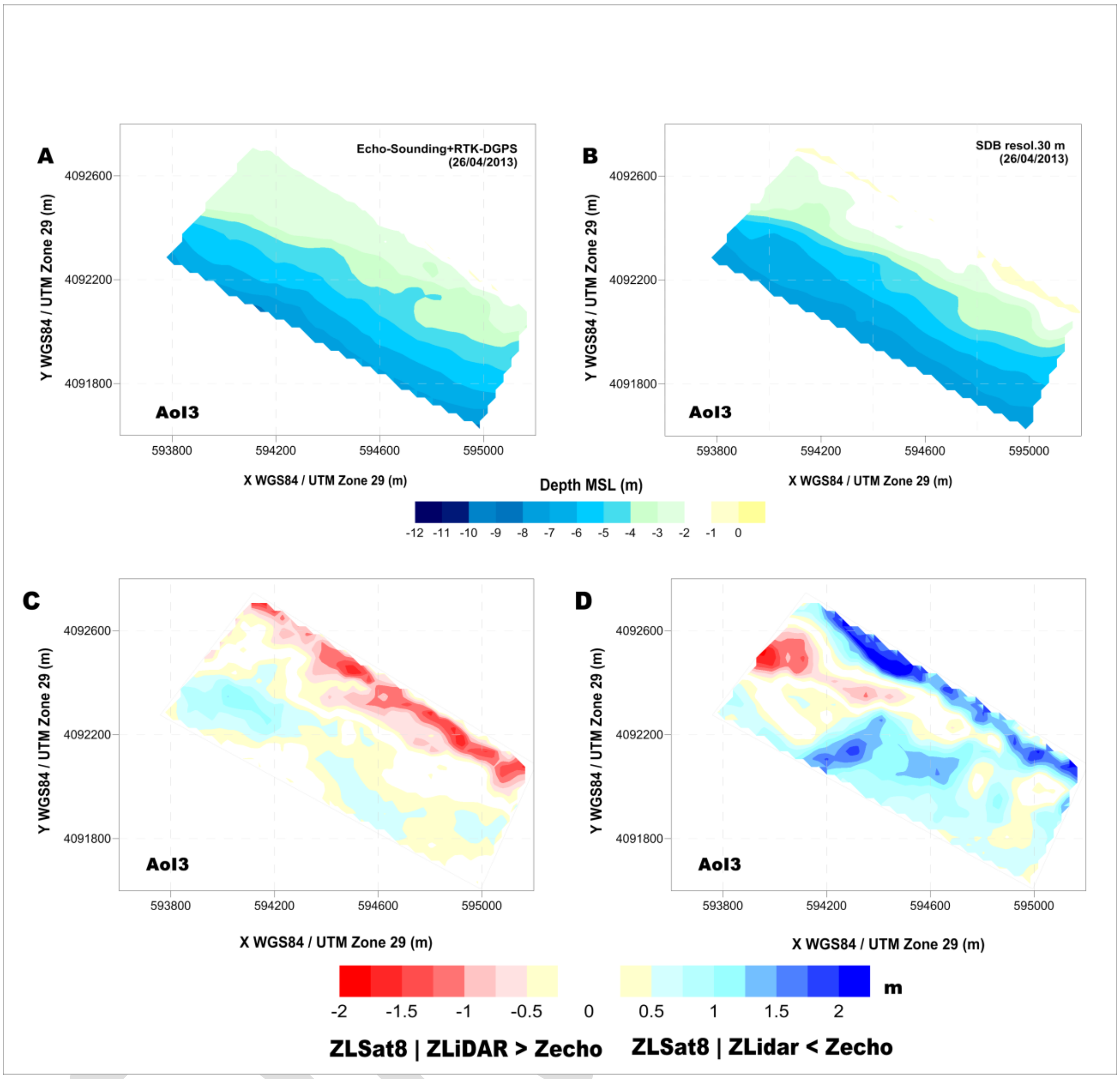

Figure 11. (A) AoI3 bathymetry contour map acquired using an echo-sounder synchronised with a RTK–DGPS in the area adjacent to Ancão Inlet on 26 April 2013. (B) Satellite-derived bathymetry (SDB) contour map (Bm3) with a 30-m resolution. (C) Difference map between A and B. (D) Difference map between LiDAR 05/2011 and SDB data derived from the Landsat 8 image of 26 April 2013; the red/blue values signify that accretion/erosion has occurred, respectively.

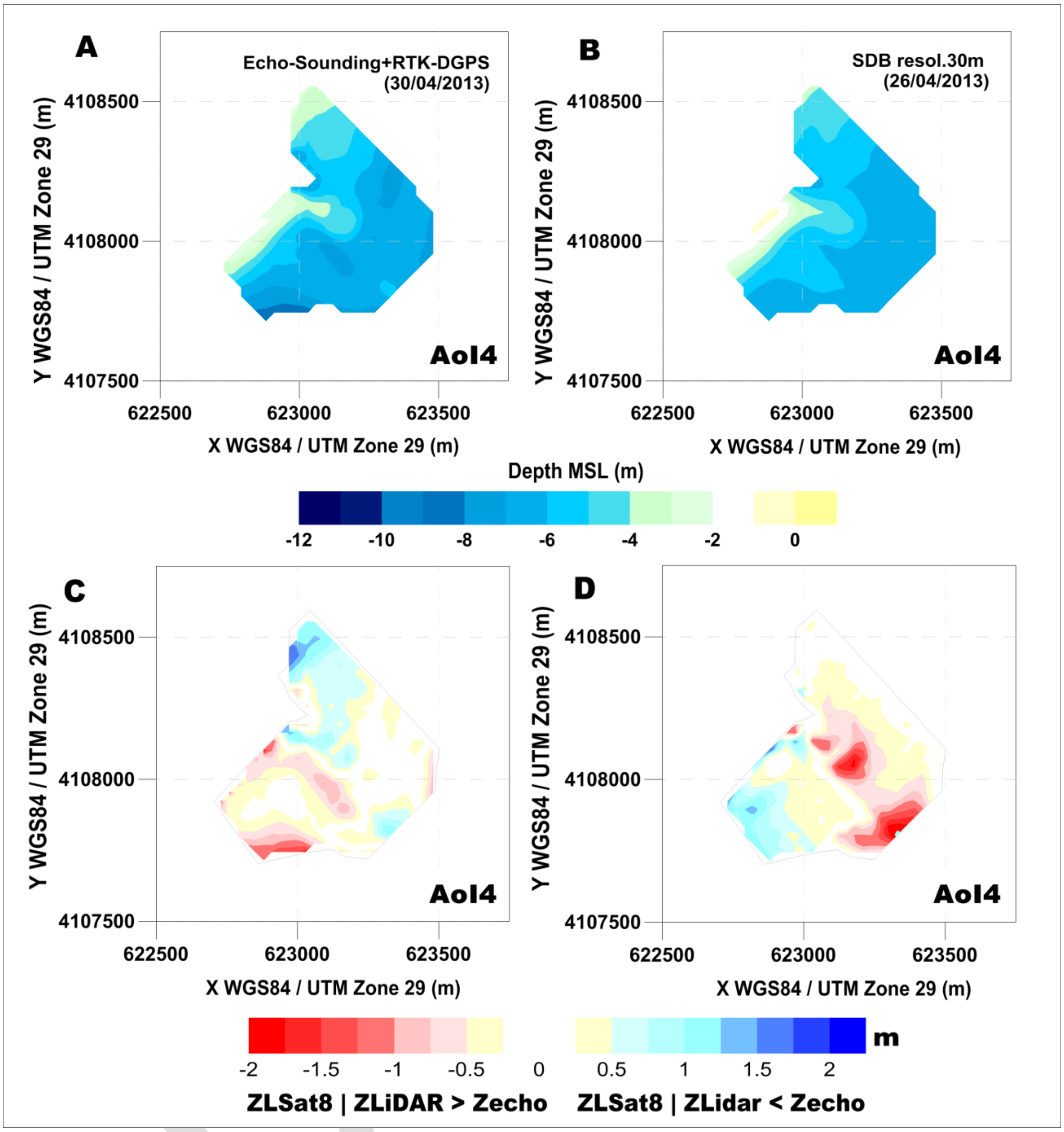

Figure 12. (A) AoI4 bathymetry contour map acquired using an echo-sounder synchronised with a RTK–DGPS in and around Tavira Inlet on 30 April 2013. (B) Satellite-derived bathymetry (SDB) contour map (Bm3) with a 30-m resolution. (C) Difference map between A and B. (D) Difference map between LiDAR 05/2011 and SDB data derived from the Landsat 8 image of 26 April 2013; the red/blue values signify that accretion/erosion has occurred, respectively.